Compressibility effect on flow characteristics over a circular cylinder at Reynolds number of 3900.

XUE, Kuiju <http://orcid.org/0009-0009-4200-7220>, LI, Qinling <http://orcid.org/0000-0002-7191-9538> and ZHAO, Liangyu <http://orcid.org/0000-0003-4513-2528>

Compressibility effect on flow characteristics over a circular cylinder at Reynolds number of 3900

XUE, Kuiju <http://orcid.org/0009-0009-4200-7220>, LI, Qinling <http://orcid.org/0000-0002-7191-9538> and ZHAO, Liangyu <http://orcid.org/0000-0003-4513-2528>

Published version

XUE, Kuiju, LI, Qinling and ZHAO, Liangyu (2024). Compressibility effect on flow characteristics over a circular cylinder at Reynolds number of 3900. Physics of Fluids, 36 (8). [Article]

Compressibility effect on flow characteristics over a circular cylinder at Reynolds number of 3900

Kuiju Xue (薛奎举),[1] Qinling Li (李勤凌),[2] and Liangyu Zhao (赵良玉)[1, a)]
[1)]*School of Aerospace Engineering, Beijing Institute of Technology, Beijing 100081, P. R. China*
[2)]*Department of Engineering and Mathematics/MERI, Sheffield Hallam University, Sheffield, S1 1WB, UK*

The compressibility effect of flow over a circular cylinder has been investigated using wall-resolved large eddy simulation. The Reynolds number in terms of the free-stream quantities and the cylinder diameter is fixed at 3900, while varying the free-stream Mach number from 0.01 to 0.5. Mesh quality, numerical scheme, and sub-grid scale model are carefully verified prior to the detailed flow study. Results such as Mach number effects on the drag coefficient, the shape of the mean streamwise velocity profile in the near wake, the length of the recirculation zone, and shear layer instability are provided. Although compressibility suppresses the Kelvin-Helmholtz instability and mixing process within the shear layer, it increases the velocity fluctuation in the boundary layer and the pressure difference between the freestream and recirculation zone, which intensifies the wake oscillation, shedding amplitude, thus shortens the recirculation zone significantly with the Mach number up to 0.5. This phenomenon is different from that found in lower Reynolds number cases where the length of the recirculation zone elongates as the Mach number increases. The deficit of the velocity profile shape in the near-wake depends on the length of the recirculation zone. Furthermore, inside the wake zone and near the cylinder back wall, two pairs of recirculation bubbles emerge as the Mach number increases.

I. INTRODUCTION

The flow field over a cylinder is simple in geometry but extremely complex in physics. Researchers have put in tremendous effort to understand its fundamental flow phenomena under different circumstances. A typical example is the compressibility effect on the wake of flow over a cylinder at low Reynolds number (Re), which has many novel applications such as high altitude flight, unmanned aerial vehicle (UAV), Mars missions, and vacuum trains[1–3]. Knowledge of the drag forces on a circular cylinder can also be used to estimate the normal force and pitching moment acting on rockets at different angles of attack[4,5]. Due to the above characteristics, the study of compressible flow over a cylinder at low Re has gained much attention recently.

In 2015, Canuto and Taira[1] performed direct numerical simulations (DNS) of compressible flows over a circular cylinder at $20 < Re < 100$ and free flow Mach number (Ma_∞) less than 0.5. Subsequently, in 2023, Rolandi et al.[3] extended the Reynolds number range to $200 \sim 350$. An isolated simulation at $Re = 3900$ and $Ma_\infty = 0.4$ was reported by Mani et al.[6] in their study of optical distortions by separated shear layers and turbulent wakes. Although Nagata et al.[2] conducted an experimental investigation with Re between 1000 and 5000 and Ma_∞ between 0.1 and 0.5 in 2022, a systematic numerical investigation of compressible flow over a cylinder at a subcritical Reynolds number of $Re = 3900$ is essential to investigate the flow mechanism behind the directional change relevant to the length of the recirculation zone. So far, there is a gap in the literature. It will be beneficial to undertake an intensive numerical work to fill in this piece of the puzzle by providing reliable three dimensional unsteady data and enhancing visual comprehension. This forms the primary motivation and objective for the current study, which focuses on the effect of compressibility at the typical subcritical Reynolds number of 3900.

Additionally, there exists a controversy concerning the incompressible and weak compressible flow over a cylinder at $Re = 3900$. The pioneering Particle Image Velocimetry (PIV) experimental set-up at this Reynolds number was meticulously detailed by Lourenco and Krothapalli[7], with results later presented by Lourenco and Shih[8] then published in a NASA technical report[9] and Beaudan's PhD thesis[10]. Their result showed the average velocity profile nearly converged into a V-shape profile at about one diameter behind the cylinder. However, Ma et al.[11] and Kravchenko and Moin[12] respectively pointed out that different simulations yielded average velocity profiles of two distinct shapes, U-shaped and V-shaped, at the identical location.Then, Parnaudeau[13] did an experiment in 2008 that showed a U-shape velocity profile at the same location, which intensified the controversy. This U-shape versus V-shape controversy persists in subsequent numerical research publications. Chen et al.[14] claimed that the magnitude of the numerical dissipation affected the shape of the velocity profile. When the numerical scheme was excessively dissipative, the velocity profile was V-shaped. Free inlet flow turbulence[15], cylinder vibration[16], and acoustic forcing[17] have also been found to be reasons for the velocity profile controversy. However, the impact of compressibility on this controversy remains unexplored. Therefore, the secondary objective of this work is to explore whether compressibility constitutes a contributing factor to the controversy.

Furthermore, Canuto and Taira[1] observed that the length of the recirculation zone extended as the Ma_∞ increased from 0 to 0.5 at $20 < Re < 100$. In contrast, Rolandi et al.[3] noted that the length of the recirculation zone remained mostly unaffected by the Ma_∞ between $200 < Re < 350$. Nagata et al.[2] demonstrated that at $Re = 2000$ and 3000, the length of the recirculation zone initially decreased then increased with the increasing Ma_∞. However, for $Re = 4000$ and 5000, the recirculation zone length decreased with Ma_∞ increase. These

[a)] Author to whom correspondence should be addressed: zhaoly@bit.edu.cn

studies collectively suggest a non-uniform response of recirculation zone length to Ma_∞ across different Reynolds numbers range. The variations in the size and configuration of the recirculation region directly correlate with the length of the vortex formation region, the dynamics of the downstream flow[12], and the stability of the shear layer. Therefore, the third objective of this study is to investigate the variations of recirculation zone length with Ma_∞ at the critical Reynolds number of $Re = 3900$ and to provide a mechanism explanation for these observed trends.

So, in the present work, wall-resolved large eddy simulation (LES) of incompressible and compressible flows over a circular cylinder with a constant $Re = 3900$ have been carried out using open source Computational Fluid Dynamics (CFD) solver OpenFOAM (Field Operation and Manipulation). In the first part of this work, simulation results of the incompressible flow over a cylinder with 5 different meshes and 5 different SGS models are verified to assess the accuracy of LES in OpenFOAM compared to limited references. Then, effects of Mach number on the physical phenomenon of flow over a circular cylinder are investigated with a constant Re of 3900, and Ma_∞ ranging from 0.2 to 0.5. Finally, a comprehensive analysis of the boundary layer development, the shear layer and wake instability, and vortex shedding in compressible flow over a cylinder are conducted to provide an explanation of the underlying physical mechanism.

The main contributions of this study are summarized as follows:

- To the best of the authors' knowledge, this is the first systematic numerical exploration of compressible flow over a cylinder at the subcritical Reynolds number of 3900. It fills a void in the literature, offers a substantial dataset, provides comprehensive visualization, and unveils novel flow phenomena.
- We initially proposed and confirmed through simulations that compressibility is one of the causes of the velocity controversy. Any cause of velocity differences corresponds to differences in the length of the recirculation zone. The variation of the recirculation zone under current conditions is also investigated.
- The mechanisms of compressible effect on the wake of flow over a cylinder are elucidated. On the one hand, the compressibility inhibits the development of velocity fluctuation in the shear layer, which delays vortex shedding; on the other hand, the pressure gradient that increases with Mach number causes vortex shedding earlier.

II. NUMERICAL APPROACHES

The wall-resolved LES is used to accurately resolve complex flow structures and physical phenomena in both incompressible (pisoFoam) and compressible (rhoPimpleFoam) flow over a cylinder. Mesh refinement, numerical scheme, and sub-grid models are tested to investigate their influence on the solution accuracy. A brief introduction to numerical methods is presented in this session.

A. Governing equations

The three-dimensional compressible Navier-Stokes (N-S) governing equations of the differential form are given by

$$\frac{\partial \rho}{\partial t} + \frac{\partial \rho u_i}{\partial x_i} = 0, \tag{1}$$

$$\frac{\partial \rho u_i}{\partial t} + \frac{\partial \rho u_i u_j}{\partial x_j} = -\frac{\partial p}{\partial x_i} + \frac{\partial \sigma_{ij}}{\partial x_j}, \tag{2}$$

$$\frac{\partial \rho e}{\partial t} + \frac{\partial \rho e u_j}{\partial x_j} + \frac{\partial q_j}{\partial x_j} = -\frac{\partial p u_i}{\partial x_i} + \frac{\partial u_i \sigma_{ij}}{\partial x_j}. \tag{3}$$

Here ρ is the density; t is the time; u_i (or u_j) is the Cartesian velocity components in x_i (x_j) direction, where $i,j = 1, 2, 3$; p is the static pressure; the viscous stress tensor is modeled for a Newtonian fluid as $\sigma_{ij} = 2\mu S_{ij} - (2/3)\mu S_{kk}\delta_{ij}$, where μ is the dynamic viscosity computed with Sutherland's law, $S_{ij} = (\partial u_i/\partial x_j + \partial u_j/\partial x_i)/2$ is the strain rate tensor and the Kronecker delta symbol, δ_{ij}, is a piecewise function with $\delta_{ij} = 1$ if $i = j$ and 0 otherwise; e is the total energy per unit volume which is defined as $e = p/[(\gamma-1)\rho] + (u_i u_i)/2$; q_j is the heat flux generated by heat conduction. For an ideal gas, pressure, p, and the static temperature, T, are linked by the equation of state $p = \rho RT$.

B. Subgrid scale models

In the LES predictions, only the large energy-carrying eddies are computed directly, whereas the influence of the small eddies has to be modeled by using a subgrid-scale (SGS) model. Consequently, the governing equations have to be filtered in space, leading to the so-called filtered N-S equations. In order to obtain a relatively simple and easily closed filtered governing equation, the Favre[18] averaging (or density based averaging) is used, so the velocity, temperature, and internal energy are indicated with a superscript "~" , while the time averaging for density and pressure are indicated with a superscript "−" . The momentum equation obtained after filtering is as follows:

$$\begin{aligned} &\frac{\partial \bar{\rho}\widetilde{u_i}}{\partial t} + \frac{\partial \bar{\rho}\widetilde{u_i}\widetilde{u_j}}{\partial x_j} = \\ &-\frac{\partial \bar{p}}{\partial x_i} + \frac{\partial \widetilde{\sigma_{ij}}}{\partial x_j} + \frac{\partial\left[\bar{\rho}\left(\widetilde{u_i u_j} - \widetilde{u_i}\widetilde{u_j}\right)\right]}{\partial x_j} + \frac{\partial(\bar{\sigma}_{ij} - \widetilde{\sigma}_{ij})}{\partial x_j}. \end{aligned} \tag{4}$$

It is similar to the original equation but contains the additional subgrid-scale stress tensor,

$$\tau_{ij} = (\widetilde{u_i u_j} - \widetilde{u_i}\widetilde{u_j}). \tag{5}$$

To enclose the filtered N-S equations, the extra unknown term will be modeled using a SGS model. In this work, five different SGS models, namely Smagorinsky (SM), DynamicSmagorinsky (DSM), k-equation (Keqn), Dynamickeqn (DKeqn), and Wall-Adapting Local Eddy-viscosity (WALE) models are tested to verify the influence of different SGS models in the near-wall and shear layer region. All five models are based on an artificial eddy viscosity approach, which treats the dissipation of kinetic energy at sub-grid scales as analogous to molecular diffusion. In this case, the SGS tensor τ_{ij} is split into an isotropic part $\frac{1}{3}\tau_{kk}\delta_{ij}$ and an anisotropic part $\tau_{ij}-\frac{1}{3}\tau_{kk}\delta_{ij}$. And τ_{ij} is modeled as:

$$\begin{aligned}\tau_{ij} &= (\tau_{ij}-\frac{1}{3}\tau_{kk}\delta_{ij})+\frac{1}{3}\tau_{kk}\delta_{ij}\\ &\approx -2\nu_{sgs}\bar{S}_{ij}+\frac{1}{3}\tau_{kk}\delta_{ij} = -2\nu_{sgs}\bar{S}_{ij}+\frac{2}{3}k_{sgs}\delta_{ij},\end{aligned} \tag{6}$$

where ν_{sgs} is the SGS viscosity and the SGS kinetic energy $k_{sgs}=\frac{1}{2}\tau_{kk}=\frac{1}{2}(\overline{u_k u_k}-\bar{u}_k\bar{u}_k)$. All eddy viscosity models are modeling the subgrid viscosity, and in OpenFOAM the subgrid scale viscosity is computed as:

$$\nu_{sgs} = C_k\Delta\sqrt{k_{sgs}}. \tag{7}$$

Here C_k is a model constant whose default value is 0.094 and Δ is the filter size that defines the subgrid length scale.

The Smagorinsky SGS model[19] is the oldest SGS model. For this model, the eddy viscosity is defined as:

$$\nu_{sgs} = C_s^2\Delta_c^2(2S_{ij}S_{ij})^{1/2}, \tag{8}$$

where C_S is the Smagorinsky constant. And in OpenFOAM

$$C_s^2 = C_k\sqrt{\frac{C_k}{C_\varepsilon}}, \tag{9}$$

where C_ε is the dissipation constant, which equals 1.048. So, the value of the Smagorinsky constant is 0.168 here. Δ_c is a geometric-based delta function $(\Delta x\Delta y\Delta z)^{1/3}$. Since there are no vortices near the wall, the Van Driest damping function is chosen here to correct the subgrid length scale. The Van Driest damping function is given by: $D=1-\exp^{-y^+/A^+}$. So the final length scale is given by: $\Delta=\min(D\kappa y/C_s,\Delta_c)$, with $A^+=26$ and $\kappa=0.41$ in OpenFOAM. The coefficients of the Smagorinsky model are determined by the isotropic equilibrium energy spectrum, but the actual complex turbulence is not uniformly isotropic. Therefore, the results of the conventional Smagorinsky model are too dissipative for the simulation of shear turbulence. So, it may underestimate the separation shear layer of the flow over a cylinder.

For the Smagorinsky model, only a single general constant is used for different turbulent fields in rotational or shear flow, near a solid wall, or in transition. For the DynamicSmagorinsky model, the coefficient is varied and determined by the local characteristics of the solvable scale pulsations. A test filter is introduced to determine a local value of the Smagorinsky constant, noted

$$\nu_{sgs} = C_d^2\Delta_c^2(2S_{ij}S_{ij})^{1/2}. \tag{10}$$

The calculation of C_d is based on Germano's identity[20] and the least-square procedure of Lilly[21]. The subgrid-scale stresses vanish in laminar flow and at a solid boundary and have the correct asymptotic behavior in the near-wall region of a turbulent boundary layer.

The WALE SGS model[22] is an algebraic eddy viscosity model (0-equation model) as with the Smagorinsky SGS model. But the WALE model relates ν_{sgs} to the rotation rate so that for an arbitrary surface, ν_{sgs} tends to zero since the rotation rate tends to zero. This makes WALE easier to implement and more stable than the Smagorinsky model. The WALE model was also validated and employed in LES supersonic jet in cross flow study[23]. For WALE model

$$\nu_{sgs} = C_w^2\Delta_c^2\frac{(S_{ij}^dS_{ij}^d)^{3/2}}{(\bar{S}_{ij}\bar{S}_{ij})^{5/2}+(S_{ij}^dS_{ij}^d)^{5/4}}, \tag{11}$$

where C_w is WALE model constant whose default value is 0.325 in OpenFOAM, $\bar{S}_{ij}=(\partial\bar{u}_i/\partial x_j+\partial\bar{u}_j/\partial x_i)/2$, S_{ij}^d is the traceless symmetric part of the square of the velocity gradient tensor, which is calculated by

$$S_{ij}^d = \frac{1}{2}(\frac{\partial\bar{u}_k}{\partial x_i}\frac{\partial\bar{u}_j}{\partial x_k}+\frac{\partial\bar{u}_k}{\partial x_i}\frac{\partial\bar{u}_j}{\partial x_k})-\frac{1}{3}\delta_{ij}\frac{\partial\bar{u}_k}{\partial x_l}\frac{\partial\bar{u}_l}{\partial x_k}. \tag{12}$$

K-equation model[24] is a one equation eddy viscosity model which also follows equation (7), and the value of model constant C_k also is 0.094. But different from the Smagorinsky model, assuming the local equilibrium to calculate k_{sgs}, the K-equation model solves a transport equation of k_{sgs}

$$\begin{aligned}\frac{\partial(\rho k_{sgs})}{\partial t}+\frac{\partial(\rho\bar{u}_j k_{sgs})}{\partial x_j}-\frac{\partial}{\partial x_j}[\rho(\nu+\nu_{sgs})\frac{\partial k_{sgs}}{\partial x_j}] =\\ \rho\tau_{ij}:\bar{S}_{ij}-C_\varepsilon\frac{\rho k_{sgs}^{3/2}}{\Delta}.\end{aligned} \tag{13}$$

Here the dissipation constant C_ε also is 1.048. This theoretically improves the accuracy of simulations of flow in jets and wake flows, as well as near the walls of channels and boundary laminar flows, where in practice the subgrid scale energy production and dissipation are not balanced.

For the DynamicKeqn model, a dynamic procedure is applied to evaluate the coefficients C_k and C_ε as given by Kim and Menon[25].

C. Numerical scheme

The implicit second-order Euler method was used for the time integration together with a fixed dimensionless time step $\Delta t/\frac{D}{U_\infty}$ to guarantee a local maximum CFL number around 0.5, where Δt is time step and U_∞ is the free stream velocity. The central difference scheme was applied for all convective term approximations. For the spatial discretization, we use the QUICK[26] scheme for incompressible cases

$$\phi_{i-\frac{1}{2}} = \frac{6}{8}\phi_{i-1}+\frac{3}{8}\phi_i-\frac{1}{8}\phi_{i-2}, \tag{14}$$

where ϕ_{i-1}, ϕ_i and ϕ_{i+1} are the fluxes at the center of the three neighboring cells, and $\phi_{i-\frac{1}{2}}$ is the flux at the cell surface.

Although the maximum freestream Ma_∞ is 0.5 in this work, the maximum local Mach number near the separation points and wake would be much larger for the flow over a cylinder. So vanLeer[27] scheme is used for compressible cases:

$$\phi_{i-\frac{1}{2}} = \phi_{i-1} + \frac{1}{2}\Psi(r)(\phi_{i-1} - \phi_{i-2}). \tag{15}$$

In OpenFOAM

$$\Psi(r) = \frac{r+|r|}{1+|r|}, \tag{16}$$

where

$$r = \begin{cases} 2 \times \dfrac{\Delta x(\nabla\phi)_{i-1}}{\phi_i - \phi_{i-1}} - 1, & \text{if} \quad \text{flux}_f > 0 \\ 2 \times \dfrac{\Delta x(\nabla\phi)_i}{\phi_i - \phi_{i-1}} - 1, & \text{if} \quad \text{flux}_f \leq 0 \end{cases}. \tag{17}$$

The compressible numerical method could also be used to solve the incompressible cases by theory, and the simulation results are in good agreement with the Mach number up to 0.2. However, the computation time is nearly doubled, so we use the QUICK scheme and piso solver for the incompressible case. In analyzing the effect of compressibility, we mainly focus on the Mach number interval from 0.2 to 0.5, and the numerical methods for these cases are consistent which are using the vanLeer scheme and rhoPimple solver.

III. COMPUTATIONAL DESCRIPTION AND SETUP

A. Computational domain and mesh design

The mesh topology and the coordinate system used in the present study of flow over a cylinder are shown in Fig.1. Here, x, y and z denote the streamwise, transverse and spanwise directions. For the computational domain, rectangular (H-type), C-type, and O-H type can be seen in different literature. However, O-type computational domains are commonly used, as they facilitate the generation of grids with high orthogonality. The radius of the O-type computational domain is represented by R. The values of R adopted in various studies span from $15D$ (Breuer[28] Case $D3$) to $60D$ (Breuer[28] Case E2), with intermediate values of $25D$ (Lysenko et al.[29]), $30D$ (Kravchenko and Moin[12]), and $35D$ (Mani et al.[6]), where D is the diameter of the cylinder. Breuer[28] conducted a comparison between the results for R values of $15D$ and $60D$ and concluded that a domain size of $R = 15D$ is fully sufficient. In the present work, an O-type computational domain with $R = 25D$ was set up for incompressible cases. The span of the computational domain is chosen πD, which is the same as that used by Kravchenko and Moin[12], Lysenko et al.[29], and Cheng et al.[30]. It was validated by Kravchenko and Moin[12], Parnaudeau et al.[13], and Breuer[28], who all claim that doubling the cylinder span from πD to $2\pi D$ and maintaining the span-wise resolution does not affect the results much.

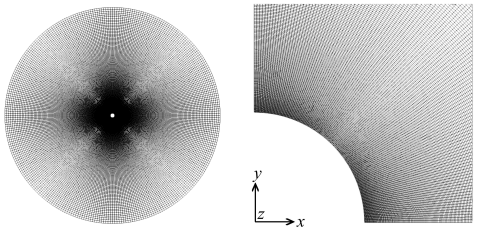

(a) (b)

FIG. 1. Description of the grid (a) and zoom into the cylinder region (b) for the incompressible flow over a cylinder

As illustrated in Kravchenko and Moin[12], the mesh resolution may have a significant effect on the velocity profile. Current work has designed five meshes from Mesh1 to Mesh5 to verify its independence and optimize the capture ability of the vortex structure in the wake region. All the meshes are curvilinear O-type orthogonal meshes. The details of all the mesh can be viewed in Table I. Here, Δr_{min}, $\Delta\theta_{min}$, and ΔZ_{min} are the cell length of the first layer near the wall in radius, circumference, and spanwise directions, respectively; N_r, N_θ and N_z are the corresponding number of cells in radius, circumference, and spanwise directions; and N_{total} is the number of the total cells. The meshes are only stretched in the radial direction, with a bias factor of f_e. This is done to avoid the occurrence of numerical inaccuracies due to unfavorable cell aspect ratios[31]. The mesh resolution near the wall and downstream of the cylinder is critical to the simulation results. In order to capture the structure of turbulence well, we need to investigate the minimum length scale for the flow to determine the minimum mesh size. The size of the largest eddies in the flow is only constrained by the physical boundaries and the cylinder diameter D can be taken as the characteristic length in the flow around the cylinder. From Kolmogorov's 1st similarity hypothesis, the size of the smallest scales, η, of the flow is determined by viscosity ν:

$$\eta = (\frac{\nu^3}{\varepsilon})^{1/4}. \tag{18}$$

Considering that:

$$\varepsilon \sim \frac{U^3}{D}, Re = \frac{UD}{\nu}, \tag{19}$$

then

$$\eta \sim \frac{D}{Re^{3/4}}. \tag{20}$$

It can be seen from the equation (20) that the minimum scale of turbulence is related to the cylinder diameter D and Reynolds number. In this work, the minimum turbulence scale η can be estimated from the above formula as ($\eta/D \sim 1/3900^{3/4} = 2 \times 10^{-3}$). So for all 5 meshes $\Delta r_{min}/D = 2 \times 10^{-3}$ is used in the current study.

TABLE I. Mesh Refinement for the circular cylinder simulation at $Re_D = 3900$

Mesh	$\Delta r_{min}/D$	N_r	f_e	N_θ	$\Delta\theta_{min}/D$	N_Z	$\Delta Z_{min}/D$	N_{total}
Mesh1	2×10^{-3}	150	1.043	152	2.0×10^{-2}	64	4.9×10^{-2}	1.46×10^{6}
Mesh2	2×10^{-3}	212	1.028	212	1.5×10^{-2}	64	4.9×10^{-2}	2.88×10^{6}
Mesh3	2×10^{-3}	300	1.018	300	1.0×10^{-2}	64	4.9×10^{-2}	5.76×10^{6}
Mesh4	2×10^{-3}	380	1.014	380	8.2×10^{-3}	80	3.9×10^{-2}	11.55×10^{6}
Mesh5	2×10^{-3}	480	1.010	480	6.5×10^{-3}	100	3.1×10^{-2}	23.04×10^{6}

To evaluate the resolution near the wall, the most important quality criteria is the distribution of the non-dimensional y^+ values defined by $y^+ = u_\tau \Delta y_c/\nu$, where $\Delta y_c = \Delta r/2$ denotes the distance of the cell center away from the wall and $u_\tau = \sqrt{\tau_w/\rho}$ describes the friction velocity. Figure. 2 depicts the y^+ distribution along the upper half wall for all meshes. The y^+ distributions along the lower and the upper half walls are symmetrical. For all meshes, the maximum value of y^+ is below 0.8, with a mean value of about 0.4. Hence, the wall is well-resolved.

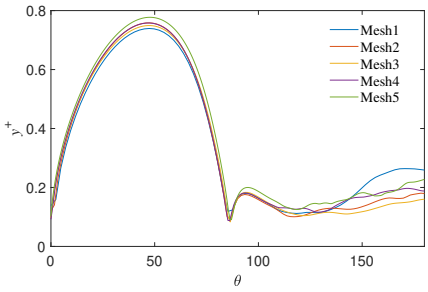

FIG. 2. Distribution of y^+ along the lower wall for different meshes

To evaluate the resolution of the region downstream of the cylinder, including the shear layer and wake regions, it is reasonable to estimate the size of the smallest scales given by the Kolmogorov length η and compared to the filter width $\Delta = (\Delta x \times \Delta y \times \Delta z)^{1/3}$ applied. In Fig. 3 (a), the profiles of δ/η at the center line of the streamwise are shown for different meshes. In Fig. 3 (b) the profiles of δ/η are shown at three different locations, $x/D = 1.06$, 1.54 and 2.02 for Mesh3, respectively. With respect to the estimation given by Pope[32] that the maximum dissipation occurs at a length scale of about 24η, these structures are resolved by at least 1–4 grid points at the streamwise center line. At $x/D = 1.06$, 1.54, and 2.02 for Mesh3, the maximum of δ/η is about 10, and thus at least more than twice smaller than the decisive scales found by Pope[32]. So, the mesh allows the resolution of a substantial part of the dissipation.

For compressible cases, the O-type computational domain is also used, and R is extended to $50D$. The inner region of $R = 25D$ is exactly the same as the incompressible case, but an additional 'sponge' layer with a thickness of $25D$ is applied

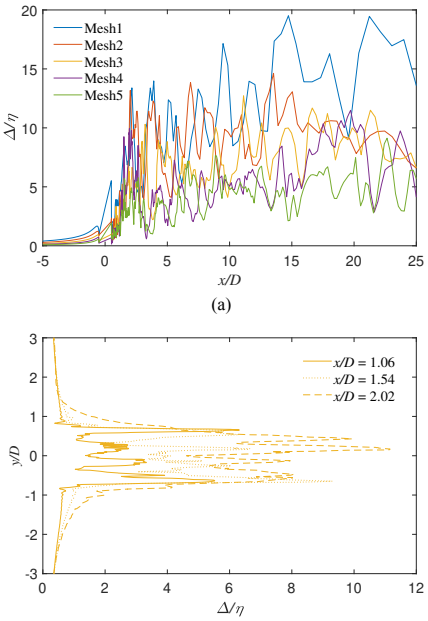

FIG. 3. (a) Profiles of Δ/η at centerline of streamwise for different meshes; (b) Profiles of Δ/η at at three different vertical positions: $x/D = 1.06$, 1.54, and 2.02 for Mesh3

at the outer boundary to damp out the flow features exiting the domain and making the boundary non-reflecting[6]. Since the mesh refinement has been validated in incompressible part, only Mesh3S (Mesh3 with 'sponge' layer), Mesh4S (Mesh4 with 'sponge' layer), and Mesh5S (Mesh5 with 'sponge' layer) are utilized with the maximum free flow Mach number case ($Ma_\infty = 0.5$).

B. Boundary conditions and other details of all test cases

For the boundary conditions, freestream velocity and pressure are used for the inlet, and the waveTransmissive outlet

TABLE II. Overview of all simulation setups for the circular cylinder

case	Ma_∞	mesh	solver	scheme	SGS	$\Delta t/\frac{D}{U_\infty}$	T_{stat}
A	0.01	Mesh1	piso	QUICK	DSM	0.002	160
B	0.01	Mesh2	piso	QUICK	DSM	0.002	160
C	0.01	Mesh3	piso	QUICK	DSM	0.002	160
D	0.01	Mesh4	piso	QUICK	DSM	0.002	160
E	0.01	Mesh5	piso	QUICK	DSM	0.002	160
F	0.01	Mesh3	piso	QUICK	SM	0.002	160
G	0.01	Mesh3	piso	QUICK	Keqn	0.002	160
H	0.01	Mesh3	piso	QUICK	WALE	0.002	160
I	0.01	Mesh3	piso	QUICK	DKeqn	0.002	160
J	0.2	Mesh3S	rhoPimple	vanLeer	DSM	0.002	160
K	0.3	Mesh3S	rhoPimple	vanLeer	DSM	0.002	160
L	0.4	Mesh3S	rhoPimple	vanLeer	DSM	0.002	160
M	0.5	Mesh3S	rhoPimple	vanLeer	DSM	0.002	160
N	0.5	Mesh4S	rhoPimple	vanLeer	DSM	0.002	160
O	0.5	Mesh5S	rhoPimple	vanLeer	DSM	0.002	160

boundary condition is utilized to avoid artificial reflections. The spanwise direction is a cyclic condition. A no-slip thermal adiabatic wall boundary condition is employed for the cylinder surface.

The convergence criteria for the main turbulence statistics vary in the literature. For internal flows, people usually use flow-through-time to account for statistical samples. However, for external flow around a cylinder, researchers normally use shedding cycles to justify it. In Kravchenko and Moin's[12] work, about seven additional shedding cycles were accumulated after a statistically stable vortex shedding was achieved. Franke and Frank[33] investigated and concluded that more than 40 shedding periods were required to achieve meaningful mean flow statistically. And simulation of Lysenko et al.[29] sampled turbulence statistics over 150 shedding cycles. In this paper, a total of 160 shedding cycles (time interval $TU_\infty/D = 800$) of turbulence data are collected for data statistics. Table II provides an overview of simulations corresponding to various kinds of meshes, SGS models, and free stream Mach numbers. All these simulations can be classified into 3 groups: 1) mesh independence is verified for incompressible and compressible simulations using all five meshes and three fine meshes for the A-E and M-O cases in Table II, respectively. The results are presented in section IV A and section IV D 1. 2) Simulations C and F-I are performed using five different SGS models, which have been presented in section II B to compare the effect of different SGS models on the results. The details will be discussed in section IV B. 3). Finally, to investigate the effect of compressibility on the flow around a cylinder, four cases with Mach numbers ranging from 0.2 to 0.5 are simulated, and further results are shown in section IV D. It should be noted that for the compressible cases J-N, the absolute dimensions of the corresponding meshes are scaled accordingly to maintain a fixed Reynolds number due to the different inflow velocities. However, the relative size of the computational domain to the cylinder diameter, the mesh topology, and the number of cells are not changed, so the scaled mesh is still referred by its original name.

IV. SIMULATION RESULTS

The simulation results of incompressible and compressible flow over a cylinder are presented in this section and are compared with some experiments[2,9,12,13,34], LES[35,36] and DNS[35].

A. Mesh independence validation of incompressible cases

For all the incompressible cases, the free stream velocity $U_\infty = 3.9m/s$, the cylinder diameter $D = 10mm$, the kinematic viscosity $\nu = 1e-5m^2/s$, which results in the freestream Reynolds number of 3900. Firstly, we investigated some mean flow characteristics, which are shown in Table III. Here, $\bar{C}_d$ represents the average drag coefficient, $C_{d_{rms}}$ and $C_{l_{rms}}$ are the root-mean-square values of the time variation of the drag and lift coefficients, θ_{sep} provides the mean flow separation angle, the basic suction coefficient is defined by $C_{P_b} = 2(P_b - P_\infty)/\rho U_\infty^2$ which is the ratio of the pressure loss behind the cylinder to the inlet flow pressure, where P_b is the pressure behind the cylinder and P_∞ is the pressure of inlet flow, St is the Strouhal number which characterizes the frequency f of vortex shedding and is defined by $St = fD/U_\infty$, the ratio of the maximum return velocity over the inlet flow velocity is $\bar{U}_{min}$, $\bar{L_{re}}/D$ is the normalized length of recirculation bubble and $\bar{L_{re}}$ is the distance from the position of the maximum return velocity to the centerline of the cylinder. For the three most important parameters describing the flow characteristics, drag coefficient, St number, and separation angle, the results of the five meshes all fall within the error range calibrated by the experimental data[12]. The Strouhal number is around 0.21 for all the current simulations, which only has a little variation in the 3rd decimal point when comparing with the experimental data[12] and empirical St–Re relationship formula[37] $St = 0.2040 + 0.3364/\sqrt{Re} \pm 0.0015$ in the certain ranges of $1300 < Re < 5000$. The value of separation angle θ_{sep} associated with different meshes is all around 86.0°. That is in good agreement with the measurement[12] where separation occurs at $\theta_{sep} = 86.0° \pm 2°$. This shows that even our coarsest mesh can accurately predict the first-order statistical results of the flow, illustrating the rationality of our mesh design and all of these five meshes can achieve excellent average results for the current simulations. Nevertheless, the relative error of the corresponding results from Mesh3 to Mesh5 is smaller. As the mesh refinement continues from Mesh3 to Mesh5, all the parameters of these three meshes converge excellently. For example, the change in the drag coefficient is only about 0.5%. Besides the fluctuating coefficients (its value is tiny, so it is prone to large relative errors), the parameter with the largest error is $\bar{L_{re}}/D$, with an error of only about 1.6%. The relative errors of all results corresponding to the three refined meshes (Mesh3, Mesh4, and Mesh5) are smaller than the relative errors of the experimental data[12]. So the results for the three fine meshes (Mesh3, Mesh4, and Mesh5) can be considered equally good for the first-order statistic.

As an important criterion for mesh resolution, the energy spectrum results in the wake region ($x/D = 3$, $y/D = 0$) are also considered and shown in Fig. 4. The first peak of the en-

TABLE III. Mesh quality effect on the mean flow parameters over a circular cylinder at $Re = 3900$

DATA	$\bar{C_d}$	$C_{d_{rms}}$	$C_{l_{rms}}$	$-C_{P_b}$	St	θ_{sep}	$\bar{U}_{min}$	$\bar{L_{re}}/D$
Data from Expt[12]	0.99 ±0.05	–	–	0.88 ±0.05	0.215 ±0.005	86.0° ±2°	−0.24 ±0.1	1.4 ±0.1
case:A(Mesh1)	0.997	0.042	0.146	0.863	0.211	86.6°	−0.287	1.44
case:B(Mesh2)	0.956	0.029	0.087	0.810	0.214	86.0°	−0.294	1.67
case:C(Mesh3)	0.948	0.032	0.083	0.800	0.212	86.1°	−0.284	1.71
case:D(Mesh4)	0.945	0.029	0.092	0.797	0.210	85.8°	−0.283	1.74
case:E(Mesh5)	0.940	0.028	0.077	0.788	0.213	85.5°	−0.285	1.77

ergy spectrum represents the vortex shedding frequency f_{vs}. The frequency of the second peak in Fig. 4 is the third shedding frequency due to the vortex alternately shedding antisymmetrically in the wake region. The numerical dissipation of Mesh1 and Mesh2 is relatively large from Fig. 4. The energy spectra of Mesh4 and Mesh5 fit the experimental data[9,13] well, even in the high frequency range. The resolution of Mesh3 in the wake is comparable to Mesh4 and Mesh5, but the number of cells is only half of Mesh4 and one-quarter of Mesh5. In addition, considering that the error between the first-order statistics for Mesh3, Mesh4, and Mesh5 discussed earlier does not exceed 1.6%, Mesh3 is good enough, and the following simulations are mainly performed with Mesh3.

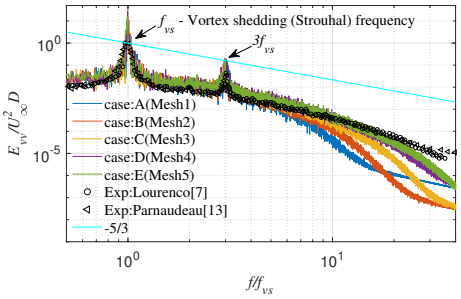

FIG. 4. Energy spectra of the transverse velocity in the wake ($x/D = 3$, $y/D = 0$)

B. U-shape versus V-shape controversy

Before discussing the results for high-resolution meshes, we note that the results for relatively coarse meshes (Mesh1 and Mesh2) are also interesting, reflecting the impact of numerical dissipation on the results. From mesh refinement (Mesh1 to Mesh3), there is one important parameter that varies significantly with mesh refinement, the length of the recirculation region ($\bar{L_{re}}/D$), which is directly related to the length of the vortex formation region and the dynamics of the downstream flow. As shown in Table III the length of the recirculation increases with the mesh refinement from 1.44 to 1.71. Xia, et al.[38] and Kravchenko and Moin[12] only varied the circumferential distribution of nodes (8, 48 respectively, with spanwise domain size as πD) and obtained different recirculation zone lengths (1.0, 1.35) when exploring the mesh effect on the results. Different from Xia et al.[38] and Kravchenko and Moin[12], all the current meshes maintain 64 nodes in the circumferential direction, with the first layer wall normal distance the same for all cases A-C, however, adapting different bias factor, f_e, in the radial direction gradually. We achieve a similar conclusion with Xia et al.[38] and Kravchenko and Moin[12] that coarser mesh corresponds to shorter recirculation region. This suggests that whichever direction the mesh becomes coarser, it results in a shorter length of recirculation region due to mesh and numerical dissipation. Because it fails to resolve the thin separated shear layers further downstream. Chen et al.[14] gave a similar opinion through the study with controlled dissipation schemes. For the three fine meshes (Mesh3 to Mesh5), the length of the recirculation gradually converges, and the relative error is only 1.6%. This shows that Mesh3 can adequately resolve the shear layer.

Figure. 5 shows the mean streamwise velocity $< u >$ along the centerline, and the velocity is averaged over time and the periodic span direction. We can clearly see that the velocity profiles of Lourenco and Shih[8] and Parnaudeau et al.[13] experiments are very different from each other within 4D, and different numerical results[35,36] don't agree with each other either. There is a big difference in the lengths of the recirculation bubble, which is determined by the position of the minimum streamwise velocity. The minimum value of the return velocity of Lourenco and Shih[8] is -0.25 at $x/D = 1.18$, but the minimum value of the return velocity of Parnaudeau et al.[13] is -0.34 at $x/D = 1.5$. This means that the recirculation zone lengths for the two experiments are 1.18 and 1.5, respectively. The longer recirculation zone corresponds to a smaller minimum recirculation velocity, and a shorter recirculation zone length corresponds to a larger minimum recirculation zone velocity. The significant difference in the results of the two experiments may be due to environmental perturbations, which shows that it is a great challenge to accurately measure the results (even the average results) of this case experimentally. Therefore, numerical research that is not affected by environmental factors emphasizes its importance. The velocity distribution corresponding to Mesh1 and Mesh3 intuitively reproduces the conclusion that a large numerical dissipation corresponds to a short recirculation flow. The velocity profiles of the three fine meshes (Mesh3 to Mesh5) completely overlap,

TABLE IV. Mean flow parameters from cylinder flow with different SGS models

DATA	$\bar{C_d}$	$C_{d_{rms}}$	$C_{l_{rms}}$	$-C_{P_b}$	St	θ_{sep}	$\bar{U}_{min}$	$\bar{L_{re}}/D$
Data from Expt[12]	0.99 ±0.05	–	–	0.88 ±0.05	0.215 ±0.005	86.0° ±2°	−0.24 ±0.1	1.4 ±0.1
case:C(DSM)	0.948	0.032	0.083	0.800	0.212	86.1°	−0.284	1.71
case:F(SM)	0.982	0.0360	0.100	0.845	0.211	86.5°	−0.250	1.54
case:G(Keqn)	0.980	0.0353	0.105	0.807	0.212	87.7°	−0.283	1.67
case:H(WALE)	0.956	0.0305	0.093	0.806	0.210	86.1°	−0.289	1.71
case:I(DKeqn)	0.949	0.0288	0.082	0.804	0.207	86.0°	−0.281	1.76

indicating the excellent convergence of the mesh.

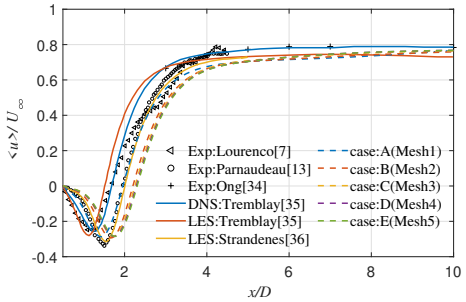

FIG. 5. Mean streamwise velocity in the wake centerline for the flow over a circular cylinder at $Re = 3900$ with different meshes

Figure. 6 shows the mean streamwise velocity at different locations in the wake at three different locations $x/D = 1.06$, $x/D = 1.54$ and $x/D = 2.02$, respectively. Note that the dimensionless velocity profiles have been shifted, and all of them should be recovered to $< u > /U_\infty = 1$ away from the cylinder. All the current velocity profiles show a U-shape in the near region behind the cylinder ($x/D = 1.06$), then gradually evolve to a V-shape downstream ($x/D = 1.54$ and $x/D = 2.02$). However, Lourenco and Shih[8] measured a V-shape profile in the very near wake $x/D = 1.06$, which contradicts most numerical simulations, including Beaudan[9], Strandenes et al.[36], and the present work at this subcritical Reynolds number, 3900. Inspired by the simulations by Xia and Karniadakis[39] on a very coarse mesh, Kravchenko and Moin[12] investigated the effect of spanwise mesh resolution effect. With a case divided into four nodes for a span length of $l_z = \pi D/2$, the V-shaped velocity profile is achieved at $x/D = 1.06$, which is consistent with the Lourenco and Shih's[8] experimental results. This under-resolved result can help us to speculate on the effect of numerical dissipation and spanwise domain size effects but is not sufficient to explain the real reason for the V-shaped velocity distribution of the experimental results at $x/D = 1.06$. This controversy is particularly aggravated by the results of the experiments at Parnaudeau et al.[13], which measured a U-shaped mean velocity profile, and all the current simulations agree with it. Combining the length of the recirculation zone in Fig. 6, we can conclude that at $x/D = 1.06$, the shorter the recirculation zone, the closer a V-shaped velocity profile, while the longer the recirculation zone, the closer U-shaped velocity profile. So, the key to the problem is the shape and length of the recirculation bubble, which is determined by the transition in the shear layers.

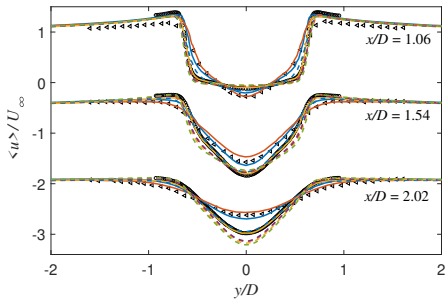

FIG. 6. Mean streamwise velocity at different locations in the wake for the flow over a circular cylinder at $Re = 3900$. See the legend for different meshes in Fig. 5

C. Performance of different SGS models

In this section, five different SGS models, such as, SM, Keqn, WALE, DKeqn, and DSM are validated with Mesh3. The different mean flow parameters are shown in Table IV. The SM and Keqn models predicted slightly higher drag coefficients than WALE, DKeqn and DSM models. Also, cases that appear to have high drag coefficients correspond to shorter return zone lengths.

In addition, the separation angle θ_{sep} of the Keqn model prediction is significantly larger than that of the other models and experiments, which can be seen from Table IV. The separation angle θ_{sep} is worked out from time-averaged wall stress distribution ($2\tau_{wall}/\rho U_\infty^2$), which is shown in Fig. 7. In addition to the slightly different separation angles, the wall shear stresses predicted by the three models (WALE, DKeqn, and DSM) completely converge with each other at a peak value of 0.067, while the Smagorinsky (SM) and Kequation (Keqn)

models overestimate the peak wall shear stress values at 0.98 and 0.9, at around $\theta = 50°$. All other four SGS models are able to predict the right flow separation point around $\theta = 86°$, except the Keqn model, which slightly overestimates the separation angle ($\theta = 87.7°$). The suction pressure coefficients ($-C_{p_b}$) are similar for all results as it is more linked to its form drag due to the shape of the cylinder. This is further proved by a similar pressure distribution around the cylinder predicted by all SGS models, apart from the SM model, which slightly underestimates the pressure on the wall in the second half of the cylinder, see it in Fig. 8.

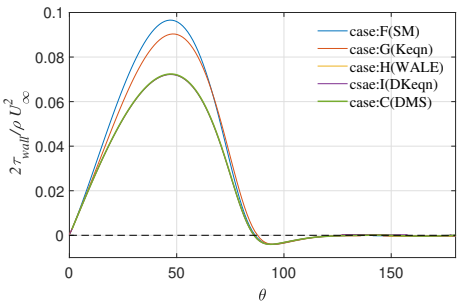

FIG. 7. Time-averaged wall stress distribution with different SGS models

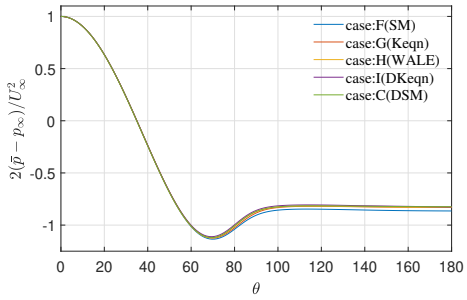

FIG. 8. Time-averaged pressure coefficient distribution for different SGS models

The performance of different SGS models in the vicinity of the wall is compared. The profiles of the tangential velocity along the wall at three locations with $\theta = 45°$, $\theta = 67.5°$ and $\theta = 90°$ are shown in Fig. 9. The results from the WALE, DKeqn, and DSM models are converged. However, the Keqn and SM models predict a slower increase in velocity within the boundary layer along the vertical direction of the wall, resulting in a thicker boundary layer and, thus, a slight increase in the distance between the upper and lower shear layers. This, in a sense, increases the blocking effect of the cylinder on the

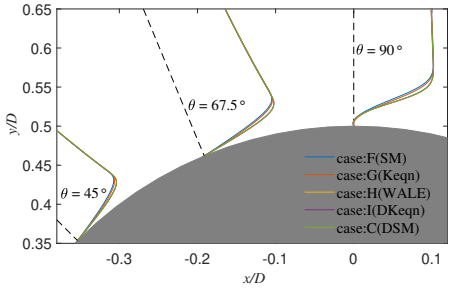

FIG. 9. Time-averaged tangent velocity profile near the wall (at $\theta = 45°$, $\theta = 67.5°$, and $\theta = 90°$)

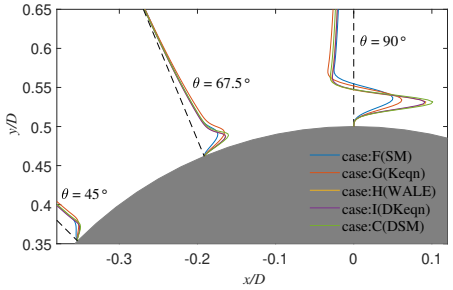

FIG. 10. Time-averaged Reynolds stress $< u'v' >$ profile near the wall (at $\theta = 45°, 67.5°$ and $90°$, respectively)

flow. And Fig. 10 shows that SM and Keqn underestimate the Reynolds shear stress at the same position.

Based on the above results, the following conclusions can be drawn: The results of the WALE model, DSM model, and DKeqn model almost overlap, and the LES results of the near-wall flow are more reasonable than those from the SM and Keqn models. In addition, the results of the first three models correspond to longer recirculation zone lengths, which indicates that the instability of the shear layer is later and the numerical dissipation is lower. In the subsequent compressible simulations in this paper, the DSM model is used.

D. Compressible flow

The simulation results of the compressible cases are presented in this section. Four different Mach numbers, ranging from 0.2 to 0.5, are considered. As introduced in section III A, for the compressible cases, the computational domain is extended to 50D. Mash3S is developed by adding a ring 'sponge' out layer with a diameter of 25D to Mash3. The mesh resolution of Mesh3S within the 25D diameter is ex-

TABLE V. Flow parameters for the Mach number of 0.5 cases with different meshes

DATA	$\bar{C_d}$	$C_{d_{rms}}$	$C_{l_{rms}}$	$-C_{P_b}$	St	θ_{sep}	$\bar{U}_{min}$	$\bar{L_{re}}/D$
case:M(Mesh3S)	1.284	0.119	0.390	1.172	0.198	87.2°/113.3°	−0.20	1.04
case:N(Mesh4S)	1.283	0.114	0.392	1.164	0.195	87.8°/112.2°	−0.23	1.03
case:O(Mesh5S)	1.288	0.108	0.390	1.205	0.197	87.4°/112.5°	−0.23	1.02

actly the same as Mesh3, except that the computational domain is increased, and a coarse mesh resolution is used in the outer layer to eliminate the artificial waves to contaminate the main flowfield we are interested in. At the same time, Mesh4S and Mesh5S are developed based on Mesh4 and Mesh5 using the same method for further mesh validation for compressible cases. The mesh quality through the interface of $25D$ is well maintained. In this part, an ideal gas is used, so the dynamic viscosity is computed with Sutherland's law and $\mu_0 = 1.71e-5\,\mathrm{kg/(m{\cdot}s)}$. As we introduced in section III B, the absolute diameters of the cylinders are scaled accordingly to maintain a fixed Reynolds number for compressible cases. For the cases of $Ma_\infty = 0.2$, 0.3, 0.4, and 0.5 the diameters of the cylinders are 0.842 mm, 0.562 mm, 0.421 mm and 0.337mm.

1. Mesh validation of compressible case

A rigorous mesh independence study is performed with a Mach number of 0.5 cases here. The extra test case N with Mesh4S and case O with Mesh5S are conducted. The mean flow parameters with three different meshes are shown in Table V. Comparing Cases M to O, almost all flow field parameters of those three compressible cases are consistent. The changes in most parameters, such as drag coefficient and s_t number, are less than 1%. In addition, The mean streamwise velocity in the wake centerline and the mean streamwise velocity at different locations in the wake are shown in Fig. 11 and Fig. 12 separately. The velocity profiles corresponding to different grids overlap almost completely, which once again confirms that the results of fine Mesh3S, Mesh4S, and Mesh5S converge with each other. So the mesh resolution of the Mesh3S is also good enough for compressible studies.

2. Overview of the main flow parameters

We will compare the Mach number effects on the flow field of a circular cylinder. As shown in Table VI, the position of the main separation point θ_{sep} moves slightly backward as the free stream Mach number increases from 0.2 to 0.5. The change is so small that it is almost negligible ($\theta_{sep} = 86°$). This can be applied to the prediction of the position of the separation point for a vehicle rocket of cylindrical cross-section flying at different angles of attack, as has been studied by Xue et al.[40], where the airflow separation point is almost constant at different angles of attack for a fixed Reynolds number and the ratio of the minimum flow velocity to the inlet flow. However, when the Mach number reaches 0.4, an attachment point appears on the

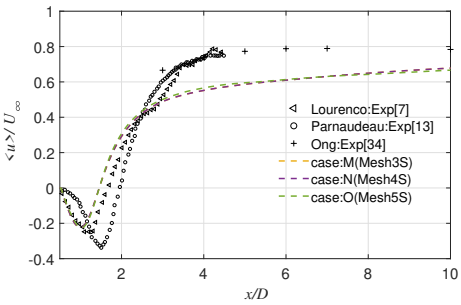

FIG. 11. Mean streamwise velocity in the wake centerline for the compressible flow ($Ma_\infty = 0.5$) over a circular cylinder at $Re = 3900$ with different meshes.

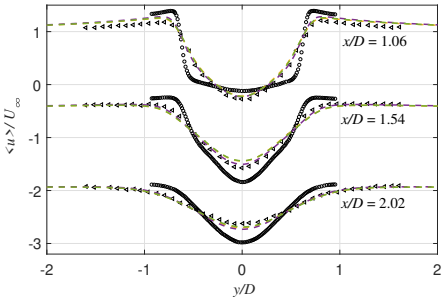

FIG. 12. Mean streamwise velocity at different locations in the wake for the compressible flow ($Ma_\infty = 0.5$) over a circular cylinder at $Re = 3900$ with different meshes. For details, see the legend of Fig.11

back wall of the cylinder, suggesting a different wake structure. The ratio of the minimum flow velocity $\bar{U_{min}}$ to the inlet flow velocity also shows a gradually decreasing trend with the increase of Mach number.

For the drag coefficient, St number, length of recirculation zone, and base suction coefficient, they are more sensitive to the changes in Mach number. The drag coefficient increases gradually with the Mach number increase. The trend of the basic suction coefficient with the increasing Mach number is basically consistent with that of the drag coefficient. Combined with the fact that the magnitude of the wall shear stress

TABLE VI. Flow parameters for compressible flow over a cylinder

DATA	$\bar{C_d}$	$C_{d_{rms}}$	$C_{l_{rms}}$	$-C_{P_b}$	St	θ_{sep}	$\bar{U}_{min}$	$\bar{L_{re}}/D$
Data from Expt[12]	0.99 $\pm$0.05	–	–	0.88 $\pm$0.05	0.215 $\pm$0.005	86.0° $\pm$2°	−0.24 $\pm$0.1	1.4 $\pm$0.1
case:C($Ma_\infty = 0.01$)	0.948	0.032	0.083	0.805	0.212	86.1°	−0.28	1.71
case:J($Ma_\infty = 0.2$)	0.982	0.037	0.115	0.851	0.208	86.1°	−0.30	1.59
case:K ($Ma_\infty = 0.3$)	1.044	0.050	0.169	0.913	0.206	86.2°	−0.28	1.49
case:L($Ma_\infty = 0.4$)	1.153	0.086	0.292	1.042	0.203	86.9°/113.4°	−0.23	1.21
case:M($Ma_\infty = 0.5$)	1.284	0.119	0.390	1.172	0.198	87.2°/113.3°	−0.20	1.04

in different cases in Fig. 18 is almost unchanged, it can be concluded that the main reason for the increase in the drag coefficient is the increase in the suction coefficient.

From Table VI, we can see that the value of the St number slightly decreases as Ma_∞ increases. This relates to the effect of different Mach numbers on vortex shedding frequency and wake stability. A lower St number corresponds to a lower vortex shedding frequency, which usually means a longer recirculation zone length. However, in Table VI, we can see that as the Mach number increases, the length of the recirculation zone shortens significantly from 1.71 to 1.04, which implies that the width of the recirculation zone increases. This will be further explained in the subsequent discussion of the wake profile, structure, and dominant flow physics.

3. *Compressible effect on the wall pressure*

Firstly, we validate the stagnation pressure for different Ma_∞. The values are shown in Fig. 13 and compering with isentropic theory:

$$C_p = \frac{p_\infty \left(\left(1 - \frac{\gamma-1}{2} \frac{U^2 - U_\infty^2}{a_\infty^2} \right)^{\left(\frac{\gamma}{1-\gamma}\right)} - 1 \right)}{1/2 \rho U_\infty^2}. \tag{21}$$

Here C_p is the pressure coefficient defined by $C_p = 2(p - p_\infty)/(\rho U_\infty^2)$ and a_∞ is the speed of sound. γ is the ratio of the specific heat capacity, and for the ideal gas, $\gamma = 1.4$. At the stagnation point $U = 0$, then equation (21) degenerates to:

$$C_{p_{stag}} = \frac{p_\infty \left(\left(1 + \frac{\gamma-1}{2} Ma^2 \right)^{\left(\frac{\gamma}{1-\gamma}\right)} - 1 \right)}{1/2 \rho U_\infty^2}. \tag{22}$$

$C_{p_{stag}}$ is the value of the pressure coefficient at the stagnation point. We can see from Fig. 13 that all the simulation data agree with the isentropic theory very well, and the value of $C_{p_{stag}}$ increases slightly as Ma_∞ increases.

Figure. 14 shows the compressible effect on the average pressure coefficient distribution along the cylinder wall. It is compared with the experimental data measured by Norberg[41] at $Re = 3000$. The horizontal axis, which shows θ, indicates the angle from the upstream stagnation point. The trend of the Mach number effect on the time-averaged pressure coefficient reverses around $\theta = 45°$ so that the pressure coefficient

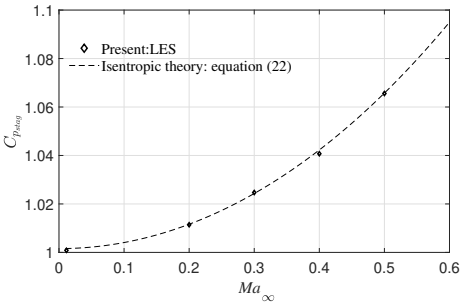

FIG. 13. Simulation and theoretical values of the pressure coefficient at the upstream stagnation point

decreases as Mach number increases for $\theta > 45°$. This kind of result can be expected from the Prandtl–Glauert transformation[42].

In addition, the Fig. 14 also clearly shows that the pressure on the back wall of the cylinder decreases as the Mach number increases, which further confirms the conclusion that the suction coefficient and drag coefficient increase with the Mach number increases.

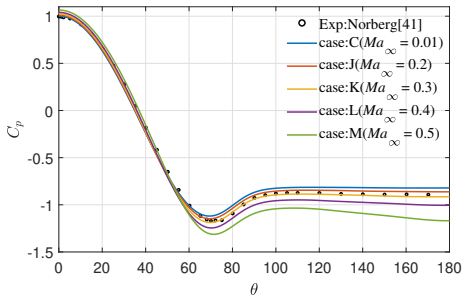

FIG. 14. Time-averaged pressure coefficient distribution for different Ma_∞

4. Compressible effect on the velocity controversy

Figure. 15 shows the Mach number effect on the mean streamwise velocity profiles in the wake centerline location. The velocity is zero at the wall of the cylinder and then reaches a negative minimum in the recirculation region and converges asymptotically to the free stream. As the Mach number increases, the minimum value of the velocity profile gradually increases, and the position, which represents the length of recirculation, advances. The simulation results with Mach number up to 0.3 closely agree with the experimental results of Parnaudeau et al.[13] but gradually become consistent with the experiments of Lourenco and Shih[8] when the free flow Mach number increases from $Ma_\infty = 0.4$ to 0.5.

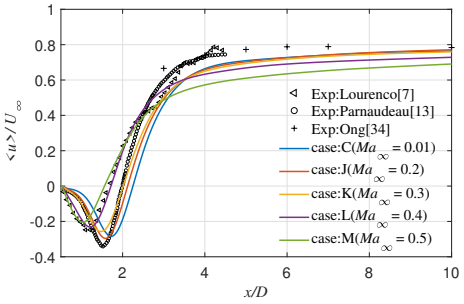

FIG. 15. Mean streamwise velocity in the wake centerline with different Ma_∞. Experiments[9,13,34] were performed under incompressible conditions with Reynolds numbers of 3900

Figure. 16 again shows the mean streamwise velocity at three different locations in the wake. The current work predicts the V-shape mean velocity profile in the near-wake region, $x/D = 1.06$ when the Mach number reaches 0.4 and 0.5. Similarly, the simulation results are close to the experimental results of Parnaudeau et al.[13] at low free flow Mach numbers ($Ma_\infty < 0.4$) and gradually becoming consistent with the experimental results of Lourenco and Shih[8] as the Mach number increases ($Ma_\infty > 0.4$) for all three wake locations. The length of the recirculation zone gradually shortens when the Mach number increases, and the velocity profile gradually transitions from a U-shape to a V-shape at the downstream location $x/D = 1.54$ and 2.02.

The experimental conditions can be very important when dealing with flow transition, such as ambient pressure, temperature, noise level, etc. Thus, the difference between the two experimental data does not mean that there is a problem with the measured data. In addition, the current work demonstrates that at $Re = 3900$, with the same wall-resolved mesh, SGS model, and inlet boundary condition, the compressibility effect does kick in after the free stream Mach number reaches above 0.4. By checking the local Mach number, it reaches a transonic flow regime (0.75) near the cylinder at $Ma_\infty = 0.5$. The Mach number will affect the instability of the wake, which

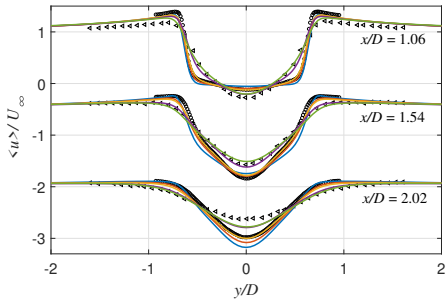

FIG. 16. Mean streamwise velocity at different locations in the wake with different Ma_∞. For details, see the legend for Fig. 15

then shortens the recirculation region and the shape of the velocity profiles (either U or V) in the very near wake of the cylinder. The previous papers only emphasized the influence of the Reynolds number on the wake, the current compressibility effect is also very significant and cannot be ignored after $Ma_\infty > 0.4$.

5. Compressible effect on recirculation zone

Figure. 17 presents the streamline and isobar of the mean velocity for the flow around the cylinder with different Mach numbers. It can be clearly seen that the length of the recirculation bubble reduces with the increase of Mach number. When the recirculation zone is long, the $x/D = 1.06$ cross-section is in the low-velocity region, and the velocity profile shows a U-shape; when the recirculation zone is short, the $x/D = 1.06$ cross-section passes through the bubble, and the velocity profile shows a V-shape. Whatever the reason for the change in the length of the recirculation zone, this difference will be shown in the velocity profile. This clearly indicates that at this sub-critical Reynolds number, the vortex shedding is advanced as the inflow velocity increases. This agrees well with the experimental results of Nagata et al.[2] at $Re = 4000$, while at a Reynolds number of 1000, the length of recirculation does not vary over a range of Mach numbers from 0.2 to 0.5. This suggests that, unlike at lower Reynolds number flow, the stability of wake flow around a cylinder at the Reynolds number of 3900 is very sensitive to the Mach number.

Also, it is worth mentioning that a secondary recirculation bubble is generated in the back of the cylinder, and it intensifies with the increasing Mach number. The mean wall stress distribution along the top half wall for different Mach numbers is shown in Fig. 18. As the Mach number increases, the maximum value of the wall shear stress increases slightly, and the location of the maximum wall stress gradually moves backward. In addition, at the Mach numbers 0.4 and 0.5, the stress appears at a new zero point on the rear wall surface. This means that apart from the main flow separation point at the

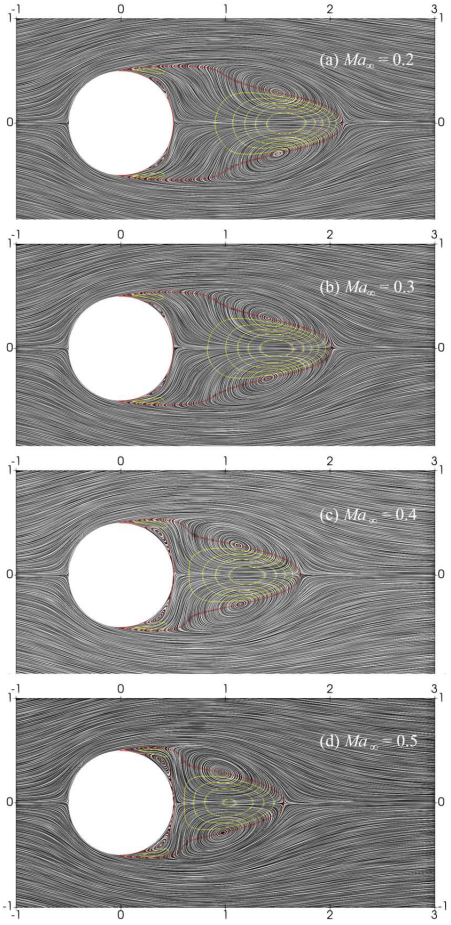

FIG. 17. Isolation line of the mean normalized velocity U/U_b and streamline of the flow around the cylinder with different Mach numbers from 0.01 to 0.5. Inside, the red line corresponds to the zero velocity profile; the yellow line is the recirculate velocity, and the difference between adjacent lines is 0.05

angle of 86°, a second flow separation point is spotted in this work, at the angle of 170°, due to the backward flow impinging on the cylinder surface. In this case, there is a small separation bubble between $\theta = 110° \sim 170°$. Similar secondary recirculations were reported in other LES studies of Breuer[28] and Tremblay[35], in which the coarse mesh resolution led to an earlier transition of the shear layer. Such flow phenomena also occur around $Re = 5000$ in experimental studies[2], ending up with a shorter recirculation bubble.

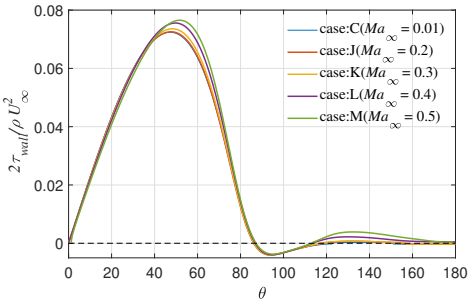

FIG. 18. Time-averaged wall stress distribution for different Ma_∞

V. MECHANISM OF COMPRESSIBILITY EFFECT

In this section, the physical mechanisms underlying the compressibility effect will be elucidated. Building upon the compressibility results outlined in the previous section, it is evident that the characteristics of the wake flow play a pivotal role in shaping the discussed flow phenomena. Consequently, this section will analyze how vortex shedding in the wake evolves with rising Mach numbers, focusing on the reasons for boundary layer development and shear layer instability. Additionally, we will examine how compressibility affects both the boundary layer and the shear layer.

A. Evolution of vortex shedding

All simulation cases are performed over 160 vortex-shedding cycles in this work. Figure. 19 shows the time histories of lift (C_l) and drag (C_d) coefficients for different cases. Although it is generally assumed that the flow can be considered fully developed after two flow through time intervals (here time interval $TU_\infty/D = 100$). In this work, the statistics starts at $TU_\infty/D = 700$, which provides enough statistically meaningful samples for data post-processing. The lift value fluctuates symmetrically up and down along the y-axis, which is caused by alternating vortex shedding with a stable frequency, while the drag coefficient shows irregular fluctuations, which may originate from the irregular three-dimensional break-up of the vortices[29]. In addition, as the Mach number increases, the fluctuation amplitudes of the lift coefficient and drag coefficient increase significantly. Although the amplitude of the lift coefficient increases dramatically with Mach number, it is still averaged around zero for a cylinder flow. The lift coefficient corresponds to the up-and-down oscillation of alternating vortex shedding. The larger the amplitude of the lift coefficient, the larger the amplitude of the wake swinging up and down. The drag coefficient is also found to increase with the Mach number. It indicates that the Mach number has a significant effect on the stability of the separating shear layers and the morphology of the

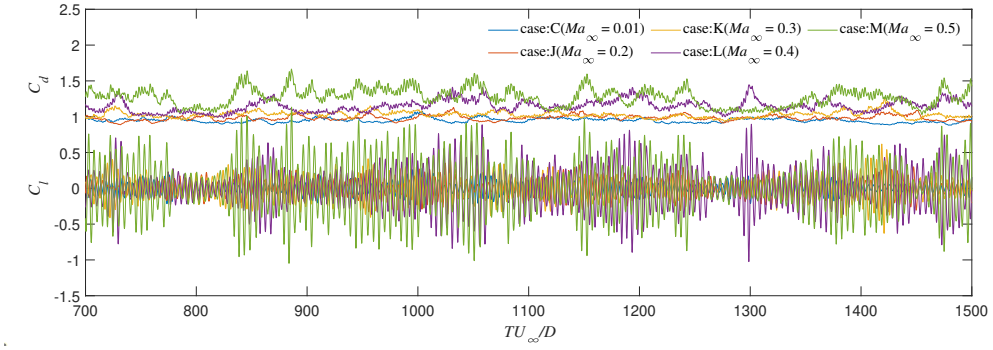

FIG. 19. Time history of the lift Cl and drag Cd coefficients of different Mach numbers

up-and-down oscillation of the vortex shedding. The energy spectra of the wake are examined. The cross-flow velocities at the wake center line ($x/D = 3$, $y/D = 0$) are sampled separately. Each site has 64 sampling points evenly distributed in the z-direction, and approximately 400,000 time series data are collected over a time interval $TU/D = 800$ at each sampling point. The spectra calculated from these time series are then averaged in the spanwise direction to increase the statistical sample. The frequency is non-dimensionalized by the Strouhal shedding frequency. Figure. 20 shows the energy spectra of different Mach numbers at the downstream location ($x/D = 3$ and $y/D = 0$) on the centreline of the wake. A -5/3 slope is also shown. At the centreline locations of the wake, the cross-flow velocity oscillates at the Strouhal frequency f_{vs}. This is simply due to the velocity distribution in the Karman vortex street. The shape of the energy spectra profiles fit well with each other for different Mach numbers at this location, however the magnitude increases with Mach number.

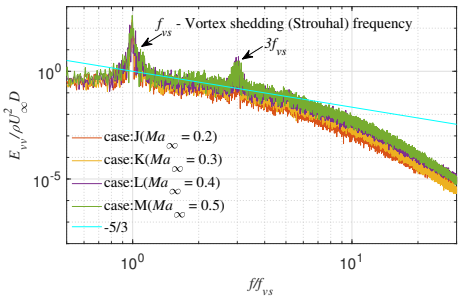

FIG. 20. Energy spectra of the transverse velocity in the wake of a circular cylinder for different Mach number, at $x/D = 3$, $y/D = 0$

Figure. 21 shows the flow structure in terms of the Q-criteria for different Mach numbers, where the dominant turbulence structure are well captured, such as, the horse shoe vortex around the cylinder and trailing vertex and their evolutions. It is colored by pressure coefficient $2(p - p_\infty)/\rho U_\infty^2$. The green color represents the low-pressure region. It can be seen from the figure that as the Mach number increases, the length of the shear layer and the recirculation zone shortens, and the width of the wake in the y direction increases. In addition, there appears to be a change in the spanwise structure angle in the far field. Vortical structures seem to be more aligned with the streamwise direction as Mach number increases. This phenomenon has been described in several shear layer simulations[43].

B. Stability of the shear layer

In order to study the effect of Mach number on the stability of the shear layer, the energy spectrum obtained by sampling at $x/D = 0.69$, $y/D = 0.69$ is shown in Fig. 22. The shear layer instability frequency (f_{SL}) (the third peak) is recorded in addition to the dominant and second shedding frequencies, which agrees with the empirical relationship formulae[44] :

$$f_{SL}/f_{vs} = 0.0235 \times Re^{0.67}. \quad (23)$$

The amplitude of the shear layer instability frequency does not increase significantly with the increase of Mach number. The ratio of the amplitude of the unstable frequency of the shear layer to the amplitude of the vortex shedding frequency decreases with the increase of Mach number, which means that the increase of Mach number suppresses the growth of the unstable frequency in the shear layer, which is consistent with the well-known studies on the stability of compressible boundary layers of plate or homogeneous shear flow[45–48], which have emerged that the stabilizing effect of compressibility on the turbulence growth increases with the increasing of Mach number in homogeneous shear flow. Therefore, at high Mach numbers, the instability in the wake flow after a cylinder is

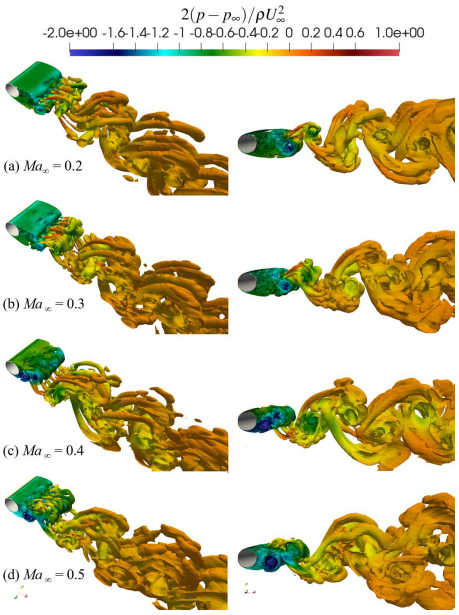

FIG. 21. Isosurfaces of instantaneous Q criteria colored by pressure

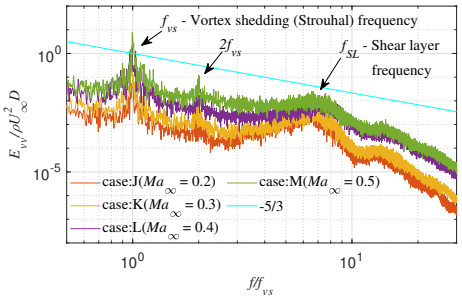

FIG. 22. Energy spectra of the transverse velocity in the wake of a circular cylinder for different Mach number, $atx/D = 0.69$, $y/D = 0.69$

not caused by a gradual increase in the perturbation within the shear layer.

Instead, the amplitude of the main frequency of vortex shedding and the second-order shedding frequency increases with Mach number. This shows that high Mach numbers intensify the wake oscillation. The normalized velocity gradient $U_g = D(\partial U/\partial y)/U$, is plotted in Fig. 23. It outlines the shape of the acceleration zone on the windward side of the cylinder and the wake region behind the cylinder. The windward side is independent of Ma_∞, but the wake region changes significantly. With the increasing Mach number, the two eddies against the back wall become obvious in Fig. 23. It is also noticed that the maximum width of the wake region moves toward the cylinder with the increasing Mach number. In addition, the amplitude of the shear layer swinging up and down increased significantly. So, at high Mach numbers, the instability in the wake flow after the cylinder is expected to be forced by the pressure difference between the freestream and vortex region, causing a stronger wake to swing up and down.

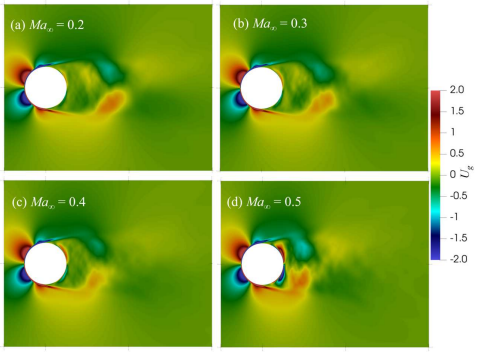

FIG. 23. The contours of normalized velocity gradient at different Mach numbers

C. The development of velocity fluctuation

The magnitude of velocity fluctuation is one of the key indicators to measure flow stability. The normalized streamwise velocity fluctuation production, $< u'u' > /U_\infty^2$, is shown in Fig. 24. At x/D =1.06 and 1.54, indicating the greater the Mach number, the greater the peak Reynolds normal stress in the shear layer. At the downstream location, x/D =2.2, the peaks of streamwise Reynolds normal stress are not significantly affected by Mach number. At the beginning of the shear layer, the amplitude of the streamwise velocity fluctuations increases dramatically with the Mach number. This indicates that flow is very sensitive at the high Mach number, which not only increases the initial disturbance in the flow direction to a certain extent but also inhibits the development of this disturbance in the shear layer.

To clarify the origin of the initial disturbance increase, the profiles of Reynolds stress $< u'u' > /U_\infty^2$ in the boundary layer at three locations with $\theta = 45°$, $\theta = 67.5°$ and $\theta = 90°$ are plotted in Fig. 25. As the flow approaches the separation point, the streamwise turbulent fluctuations in the boundary layer increase dramatically with increasing Mach number. This injects higher initial turbulence disturbance into the shear layer for the high Mach number case, corresponding to the greater peaks in Fig. 24. That is the reason why the local intensity

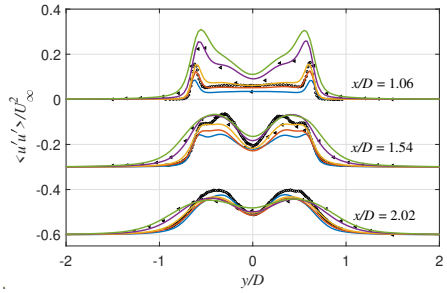

FIG. 24. Variance of the streamwise velocity fluctuations at three locations. For details, see the legend for Fig. 15

of the streamwise velocity fluctuations is higher in the nearest wake station at high Mach number.

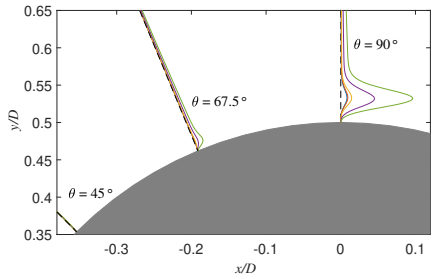

FIG. 25. Variance of the streamwise velocity fluctuations in the boundary (at $\theta = 45°, 67.5°$ and $90°$, respectively). For details, see the legend for Fig. 15

The variance of vertical velocity fluctuation, $< v'v' > /U_\infty^2$ in the wake, is shown in Fig. 26. Likewise, at the beginning of the wake, the amplitude of the fluctuations in the vertical velocity increases with Mach number from 0.01 to 0.5, and this fluctuation is found to be intensified downstream for all cases. The $< u'u' > /U_\infty^2$ and $< v'v' > /U_\infty^2$ contribute to the turbulent kinetic energy, and it is found that $< v'v' > /U_\infty^2$ changes more dramatically compared with $< u'u' > /U_\infty^2$. The results also indicate there is turbulence production around the shear layer due to flow separation and the center of the wake zone due to flow recirculation. At low Mach numbers, the amplitude of the fluctuation continues to increase from position 1.06 to 2.02, while for high Mach numbers, the disturbance increases rapidly between 1.06 and 1.54 and then slows down. This shows that for high Mach number cases, the amplitude of the wake oscillation is larger near the cylinder and the vortex shedding occurs in advance. Note the plots in both Fig. 24 and Fig. 26 are shifted for the different y/D locations to make it easy to view. The $< u'u' > /U_\infty^2$ and $< v'v' > /U_\infty^2$ values

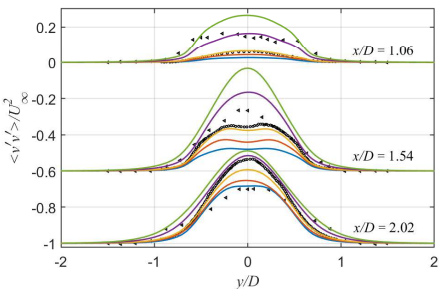

FIG. 26. Variance of the normal velocity fluctuations at three locations. For details, see the legend for Fig. 15

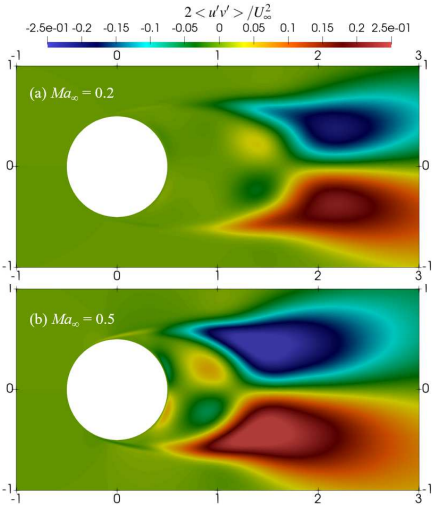

FIG. 27. The contour of $2 < u'v' > /U_\infty^2$ for $Ma_\infty = 0.2$ (up) and $Ma_\infty = 0.5$ (down)

should trend to zero far away from the cylinder.

The contours of Reynolds shear stress of $2 < u'v' > /U_\infty^2$ for the weakly compressible case at Mach numbers of 0.2 and compressible case at Mach numbers of 0.5 are shown in Fig. 27. Due to sufficient statistical samples, the contours are perfectly asymmetric. Clearly, the recirculation zone is compressed and pushed back towards the cylinder significantly with the Mach number increase. At $Ma_\infty = 0.5$, it is found another pair of recirculation bubbles close to the back wall in the wake region, which corresponds to the second flow separation point around the cylinder (see it in Fig. 18).

The turbulent kinetic energy (TKE = $(< u'u' > + < v'v' > + < w'w' >)/2$) in the wake region is normalized and shown in Fig. 28, which provides a different view of the statistical

shedding range of the shear layers and wake at $Ma_\infty = 0.2$ and 0.5. The angle of the shear layer oscillation increases with the increasing Mach number, and in the meantime, the recirculation zone decreases. For the case at $Ma_\infty = 0.2$, the TKE mainly occurs at the location where the vortex shedding starts. While for the case with Mach number 0.5, the TKE increases significantly in the shear layer as well. And the recirculation wake zone is pushed back towards the cylinder. The opening angle of the shear layer is clearly expanded downstream, which increases the width of the wake region.

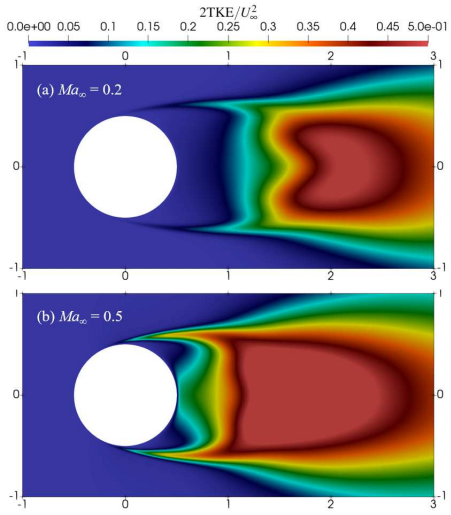

FIG. 28. Turbulent kinetic energy for $Ma_\infty = 0.2$ (up) and $Ma_\infty = 0.5$ (down)

D. Transportation with pressure gradient

Since compressibility inhibits the development of velocity fluctuations in the shear layer and thus plays a stabilizing role, one reason for increasing the amplitude of the wake oscillations may be the change in the pressure gradient. Then, we defined the relation between the convection term and pressure gradient (RCP) as the production of the convection term and pressure gradient:

$$RCP = \rho^* {u_j}^* \frac{\partial {u_i}^*}{\partial {x_j}^*} \frac{\partial p}{\partial {x_i}^*}. \tag{24}$$

It shows how the fluid microclusters transport with pressure gradient. Here $\rho^* = \rho/\rho_\infty$, ${u_i}^* = u_i/u_{i\infty}$, ${u_j}^* = u_j/u_{j\infty}$, ${x_i}^* = x_i/D$, ${x_j}^* = x_j/D$.

Figure. 29 shows that the increase in Mach number increases the pressure gradient between the two sides of the

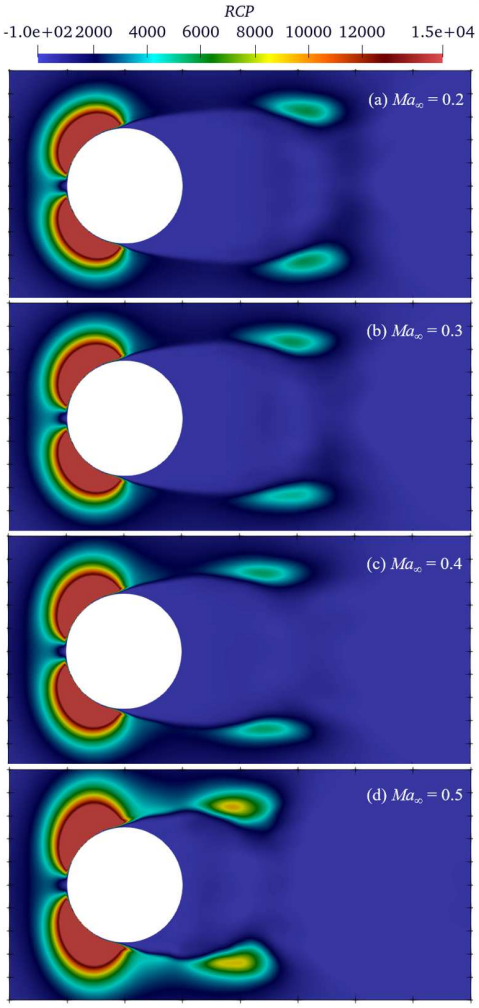

FIG. 29. Contour of particle transport with pressure gradient

shear layer. Then, the outflow squeezes the shear layer towards the center line ($y/D = 0$). The shear layer bending location is also linked to an increasing turbulent kinetic energy (Fig. 28) and shear stress (Fig. 27). The mechanism of this significantly shortened recirculation zone is due to the increasing pressure difference between the freestream and the recirculation zone, which intensifies the shear layer instability after flow separates from the curvilinear surface. A strong rolling vortex, with increasing turbulence energy production, moves up and down around the centreline ($y/D = 0$). The higher

Mach number, the greater amplitude of the vortex shedding. It statistically achieves an antisymmetric pair of vortex in the far field of the recirculation zone. The antisymmetric vortex moves towards the back of the cylinder as the Mach number increases. This is contrary to the effect that compressibility reduces the mixing in the shear layer and suppresses the Kelvin Helmholtz instability, thus delaying the instability of the shear layer and the onset of vortex shedding. The results of these two mechanisms acting alone are opposite, so whichever mechanism is dominant in the flow, the final result will show the result corresponding to that mechanism. Under low Reynolds number conditions, the pressure gradient does not change significantly with compressibility, and the compression response plays a dominant role in the stabilization effect of the shear layer and increases the length of the recirculation zone. In a certain Reynolds number range, the effects of the two mechanisms are quite offset, and the length of the recirculation zone hardly changes with the Mach number. When the Reynolds number is greater than a certain value, the increase in pressure gradient becomes significant, and vortex shedding occurs earlier with the increase in Mach number, so the length of the recirculation zone becomes shorter.

VI. CONCLUSIONS

Mach number effects on the flow characteristics over a circular cylinder have been carried out using wall-resolved LES at the subcritical Reynolds number of 3900, covering a Mach number range from 0.01 to 0.5. High-quality mesh design, low-dissipation numerical schemes, and proper SGS model are critical for accurate numerical simulation of flow over a cylinder. By addressing a research gap, this work offers reliable simulation data and visualization for the study of compressible flow over a cylinder at the subcritical Reynolds number 3900.

Compared with the incompressible flow, the compressible flow over a cylinder exhibits four significant variations with the increasing Mach number: 1) the mean drag coefficient $\bar{C}_d$, pressure coefficient $-\bar{C}_{P_b}$ and amplitude of lift coefficient fluctuation increase; 2) the velocity profile transitions from a U-shape to a V-shape at the position of $x/D = 1.06$; 3) the recirculation zone shortens and widens, and the recirculation bubbles approaches the cylinder, gradually; 4) for Mach numbers above 0.4, a new pair of recirculation bubbles forms near the back wall of the cylinder.

An intrinsic linkage exists among these significant changes in flow characteristics. The recirculation zone comprises a low-velocity region between two shear layers and two antisymmetric bubbles, the position of which depends on the vortex shedding. With the increasing Mach number, the advancement of vortex shedding propels the recirculation bubble forward, reducing the length of the low-velocity zone between the shear layers. The length of the recirculation zone determines the shape of the cross-section velocity profile at $x/D = 1.06$, displaying a U-shape when the length of the recirculation is long and a V-shape when the length of the recirculation is short. As Mach number rises, the recirculation zone progressively shortens until the recirculation bubble attaches the back wall of the cylinder, leading to flow separation and the formation of a new pair of bubbles. Furthermore, the amplitude of the upward and downward vortex shedding oscillation amplifies with Mach number, causing an escalation in an increase in the mean drag coefficient $\bar{C}_d$ and an increase in the amplitude of the lift coefficient. Consequently, the vortex shedding plays a crucial role in all these dynamic phenomena.

Compressibility affects vortex shedding through two physical mechanisms: 1) compressibility reduces the mixing in the shear layer and suppresses the Kelvin Helmholtz instability, thus delays the instability of the shear layer and the vortex shedding; 2) compressibility increases velocity fluctuation in the boundary layer and the pressure gradient in the wake region, especially the pressure difference between the freestream and the recirculation zone, leading to intensified wake oscillations and premature vortex shedding. The outcomes from these mechanisms are conflicting; therefore, the dominant mechanism determines the final results. This also explains the distinct responses of recirculation zone length to Mach numbers under different Reynolds number, as observed in the existing literature.

ACKNOWLEDGMENTS

This work has been carried out with the support of the National Science Foundation of China (No. 12072027 and No. 11532002), the Henan Key Laboratory of General Aviation Technology (No. ZHKF-230201), the Funding for the Open Research Project of the Rotor Aerodynamics Key Laboratory (No. RAL20200101), and China Scholarship Council. In addition, Professor Michael Manhart of the Technical University of Munich provided valuable input to this work. Part of computing time for the project was granted by the Leibniz Supercomputing Centre on its Linux Cluster.

[1]D. Canuto and K. Taira, "Two-dimensional compressible viscous flow around a circular cylinder," J. Fluid Mech. **785**, 349–371 (2015).
[2]T. Nagata, A. Noguchi, K. Kusama, T. Nonomura, A. Komuro, A. Ando, and K. Asai, "Experimental investigation on compressible flow over a circular cylinder at Reynolds number of between 1000 and 5000," J. Fluid Mech. **893**, A13 (2020).
[3]L. V. Rolandi, J. Fontane, T. Jardin, J. Gressier, and L. Joly, "Compressibility effects on the secondary instabilities of the circular cylinder wake," J. Fluid Mech. **966**, A36 (2023).
[4]L. H. Jorgensen, "Prediction of static aerodynamic characteristics for space-shuttle-like and other bodies at angles of attack from 0 deg to 180 deg," Tech. Rep. (NASA, No. TN-D-6996, 1973).
[5]L. H. Jorgensen, "A method for estimating static aerodynamic characteristics for slender bodies of circular and noncircular cross section alone and with lifting surfaces at angles of attack from 0 deg to 90 deg," Tech. Rep. (NASA, No. A-4700, 1973).
[6]A. Mani, P. Moin, and M. Wang, "Computational study of optical distortions by separated shear layers and turbulent wakes," J. Fluid Mech. **625**, 273–298 (2009).
[7]L. Lourenco and A. Krothapalli, "Application of pidv to the study of the temporal evolution of the flow past a circular cylinder," Laser Anemometry in Fluid Mechanics **3**, 161–178 (1986).
[8]L. M. Lourenco and C. Shih, "Characteristics of the plane turbulent near wake of a circular cylinder, a particle image velocimetry study," published in Ref. 6 (1994).

[9]P. Beaudan and P. Moin, "Numerical experiments on the flow past a circular cylinder at sub-critical Reynolds number," Tech. Rep. (NASA Ames/Stanford University, No. TF-62, 1994).
[10]P. B. Beaudan, *Numerical experiments on the flow past a circular cylinder at sub-critical Reynolds number* (Stanford University, 1995).
[11]X. Ma, G.-S. Karamanos, and G. Karniadakis, "Dynamics and low-dimensionality of a turbulent near wake," J. Fluid Mech. **410**, 29–65 (2000).
[12]A. G. Kravchenko and P. Moin, "Numerical studies of flow over a circular cylinder at Re_D = 3900," Phys. Fluids **12**, 403–417 (2000).
[13]P. Parnaudeau, J. Carlier, D. Heitz, and E. Lamballais, "Experimental and numerical studies of the flow over a circular cylinder at Reynolds number 3900," Phys. Fluids **20**, 085101 (2008).
[14]H. Chen, Z. Li, and Y. Zhang, "U or V shape: Dissipation effects on cylinder flow implicit large-eddy simulation," AIAA J. **55**, 459–473 (2017).
[15]J. Gerrard, "The mechanics of the formation region of vortices behind bluff bodies," J. Fluid Mech. **25**, 401–413 (1966).
[16]C. Chyu and D. Rockwell, "Near-wake structure of an oscillating cylinder: effect of controlled shear-layer vortices," J. Fluid Mech. **322**, 21–49 (1996).
[17]G. S. Cardell, *Flow past a circular cylinder with a permeable wake splitter plate* (California Institute of Technology, 1993).
[18]A. Favre, "The equations of compressible turbulent gases," Tech. Rep. (Annual Summary Report AD0622097, 1965).
[19]J. Smagorinsky, "General circulation experiments with the primitive equations: I. The basic experiment," Mon. Weather Rev. **91**, 99–164 (1963).
[20]M. Germano, U. Piomelli, P. Moin, and W. H. Cabot, "A dynamic subgrid-scale eddy viscosity model," Phys. Fluids A **3**, 1760–1765 (1991).
[21]D. K. Lilly, "A proposed modification of the Germano subgrid-scale closure method," Phys. Fluids A **4**, 633–635 (1992).
[22]F. Nicoud and F. Ducros, "Subgrid-scale stress modelling based on the square of the velocity gradient tensor," Flow, Turbul. Combust. **62**, 183–200 (1999).
[23]M. Zhao, T. Ye, and Q. Li, "Large-Eddy simulations of transverse jet mixing and flame stability in supersonic crossflow," AIAA J. **59**, 2126–2142 (2021).
[24]A. Yoshizawa, "Statistical theory for compressible turbulent shear flows, with the application to subgrid modeling," Phys. Fluids **29**, 2152–2164 (1986).
[25]W.-W. Kim and S. Menon, "A new dynamic one-equation subgrid-scale model for large eddy simulations," in *33rd aerospace sciences meeting and exhibit, Reno, NV, No. 95–0356* (1995).
[26]B. P. Leonard, "A stable and accurate convective modelling procedure based on quadratic upstream interpolation," Comput. Meth. Appl. Mech. Eng. **19**, 59–98 (1979).
[27]B. Van Leer, "Towards the ultimate conservative difference scheme. II. Monotonicity and conservation combined in a second-order scheme," J. Comput. Phys. **14**, 361–370 (1974).
[28]M. Breuer, "Large eddy simulation of the subcritical flow past a circular cylinder: numerical and modeling aspects," Int. J. Numer. Methods Fluids **28**, 1281–1302 (1998).
[29]D. A. Lysenko, I. S. Ertesvåg, and K. E. Rian, "Large-eddy simulation of the flow over a circular cylinder at Reynolds number 3900 using the OpenFOAM toolbox," Flow, Turbul. Combust. **89**, 491–518 (2012).
[30]W. Cheng, D. Pullin, R. Samtaney, W. Zhang, and W. Gao, "Large-eddy simulation of flow over a cylinder with: a skin-friction perspective," J. Fluid Mech. **820**, 121–158 (2017).
[31]J. Wissink and W. Rodi, "Numerical study of the near wake of a circular cylinder," Int. J. Heat Fluid Flow **29**, 1060–1070 (2008).
[32]S. B. Pope, *Turbulent flows* (Cambridge university press, 2000).
[33]J. Franke and W. Frank, "Large eddy simulation of the flow past a circular cylinder at Re_D= 3900," J. Wind Eng. Ind. Aerod. **90**, 1191–1206 (2002).
[34]L. Ong and J. Wallace, "The velocity field of the turbulent very near wake of a circular cylinder," Exp. Fluids **20**, 441–453 (1996).
[35]F. Tremblay, *Direct and large-eddy simulation of flow around a circular cylinder at subcritical Reynolds numbers*, Ph.D. thesis, Technische Universität München (2002).
[36]H. Strandenes, B. Pettersen, H. I. Andersson, and M. Manhart, "Influence of spanwise no-slip boundary conditions on the flow around a cylinder," Comput. Fluids **156**, 48–57 (2017).
[37]U. Fey, M. König, and H. Eckelmann, "A new Strouhal–Reynolds-number relationship for the circular cylinder in the range $47 < Re < 2 \times 10^5$," Phys. Fluids **10**, 1547–1549 (1998).
[38]Z. Xia, Z. Xiao, Y. Shi, and S. Chen, "Mach number effect of compressible flow around a circular cylinder," AIAA J. **54**, 2004–2009 (2016).
[39]M. Xia and G. E. Karniadakis, "The spectrum of the turbulent near-wake: a comparison of DNS and LES," in *Second AFOSR International Conference on DNS/LES, Ruston, LA* (1997).
[40]K. Xue, L. Zhao, Q. Li, and L. Jiao, "Wall temperature and rotation rate effects on the Magnus force of a spinning rocket," Heat Transfer Eng. **43**, 754–770 (2022).
[41]C. Norberg, "An experimental investigation of the flow around a circular cylinder: influence of aspect ratio," J. Fluid Mech. **258**, 287–316 (1994).
[42]H. Glauert, "The effect of compressibility on the lift of an aerofoil," Proceedings of the Royal Society of London. Series A, Containing Papers of a Mathematical and Physical Character **118**, 113–119 (1928).
[43]J. B. Freund, S. K. Lele, and P. Moin, "Compressibility effects in a turbulent annular mixing layer. part 1. turbulence and growth rate," Journal of Fluid Mechanics **421**, 229–267 (2000).
[44]A. Prasad and C. H. Williamson, "The instability of the separated shear layer from a bluff body," Phys. Fluids **8**, 1347–1349 (1996).
[45]P. Bradshaw, "Compressible turbulent shear layers," Annu. Rev. Fluid Mech. **9**, 33–52 (1977).
[46]D. Papamoschou and A. Roshko, "The compressible turbulent shear layer: an experimental study," J. Fluid Mech. **197**, 453–477 (1988).
[47]S. Sarkar, "The stabilizing effect of compressibility in turbulent shear flow," J. Fluid Mech. **282**, 163–186 (1995).
[48]G. Kumar, R. L. Bertsch, and S. S. Girimaji, "Stabilizing action of pressure in homogeneous compressible shear flows: effect of mach number and perturbation obliqueness," J. Fluid Mech. **760**, 540–566 (2014).